

JGR Solid Earth



RESEARCH ARTICLE

10.1029/2022JB025463

Magma Flow Patterns in Dikes: Observations From Analogue Experiments

Stephen Pansino^{1,2} , Adel Emadzadeh^{3,4} , and Benoit Taisne^{1,3} 

¹Earth Observatory of Singapore, Nanyang Technological University, Singapore, Singapore, ²Department of Earth Sciences, Durham University, Durham, UK, ³Asian School of the Environment, Nanyang Technological University, Singapore, Singapore, ⁴Department of Mechanical Engineering, University of Melbourne, Parkville, VIC, Australia

Key Points:

- In isothermal, buoyantly propagating dikes, a dike's internal flow ascends, whereas in source-pressure controlled dikes, it circulates
- Solidification generates a conduit in the dike tail, which acts as a high velocity point source to the head, promoting circulation
- Erupting dikes assume a simple ascending flow pattern, as liquid flow directly from the source to surface

Supporting Information:

Supporting Information may be found in the online version of this article.

Correspondence to:

S. Pansino,
stephen.g.pansino@durham.ac.uk;
steve.pansino@gmail.com

Citation:

Pansino, S., Emadzadeh, A., & Taisne, B. (2023). Magma flow patterns in dikes: Observations from analogue experiments. *Journal of Geophysical Research: Solid Earth*, 128, e2022JB025463. <https://doi.org/10.1029/2022JB025463>

Received 23 AUG 2022

Accepted 23 FEB 2023

Author Contributions:

Conceptualization: Stephen Pansino, Benoit Taisne
Data curation: Stephen Pansino, Adel Emadzadeh
Formal analysis: Stephen Pansino, Adel Emadzadeh, Benoit Taisne
Funding acquisition: Benoit Taisne
Methodology: Stephen Pansino, Adel Emadzadeh
Project administration: Benoit Taisne
Resources: Benoit Taisne
Software: Adel Emadzadeh
Supervision: Benoit Taisne
Validation: Stephen Pansino, Adel Emadzadeh
Visualization: Stephen Pansino

© 2023. The Authors.

This is an open access article under the terms of the [Creative Commons Attribution License](https://creativecommons.org/licenses/by/4.0/), which permits use, distribution and reproduction in any medium, provided the original work is properly cited.

Abstract We conducted analogue experiments to examine flux-driven and buoyancy-driven magma ascent, which included a series of isothermal experiments and thermal, solidification-prone experiments. We measured the internal flow using 2D particle image velocimetry, which indicates that buoyancy has a strong control on the flow pattern of isothermal dikes. Dikes that are not buoyant (likely driven by source pressure) take on a circulating pattern, while buoyant dikes assume an ascending flow pattern. Solidification modifies the flow field so that flow is confined to the dike's upper head region. The lower tail becomes mostly solidified, with a narrow conduit connecting the source to the head. We interpret that this conduit acts as a high velocity point source to the head, promoting a circulating flow pattern, even as the dike becomes buoyant. We then perform particle tracking velocimetry on several particles to illustrate the complexity of their paths. In a circulating flow pattern, particles rise to the top of the dike, descend near the lateral edge, and then are drawn back into the upward flow. In an ascending pattern, particles ascend slightly faster than the propagation velocity, and therefore are pushed to the side as they approach the upper tip. In erupting dikes, particles simply flow to the vent. In the context of crystal growth in magmatic dikes, these results suggest that crystal growth patterns (e.g., normal or oscillatory zoning) can reflect the magma flow pattern, and potentially the driving forces.

Plain Language Summary Dikes are magma-filled cracks, which grow through the earth and can feed volcanic eruptions. Depending on the forces acting on the magma, including buoyancy, the magma inside can flow in different ways. We studied the flow inside of dikes using small, laboratory experiments. We injected oil, water, or liquid gelatin, mimicking the magma, into a block of transparent gelatin, mimicking the Earth's crust. We added small tracer particles to the liquids, which could be tracked using cameras, to understand the flow inside of our experiments. We found that when buoyancy is low, for example, when dikes are small, the internal flow circulates up and down. However, as the buoyancy increases, they begin to flow upward. These results can be related to small crystals that form in magma in nature and record chemical information in layers (known as zoning), like rings in a tree. If a crystal circulates up and down, it can look different from one that just rises up. Such crystals may give us information about the forces that control dikes at volcanoes.

1. Introduction

Magma migration toward the Earth's surface commonly occurs through sills and dikes, which are mechanically efficient for fluid transport (Keating et al., 2008). Traditionally, dikes have been assumed to have a relatively simple internal laminar flow velocity profile, in which magma flows unidirectionally forward (either upward for ascending dikes or horizontally for laterally propagating dikes). However, it is recently becoming clear that dikes can exhibit internal flow complexities that challenge this assumption of unidirectional flow (Albert et al., 2020; Kavanagh et al., 2018).

Kavanagh et al. (2018) demonstrated, through analogue experiments, that a propagating dike has a dynamic flow pattern, which evolves in stages. Using particle image velocimetry (PIV), they found that the internal flow has a circulating pattern, in which the liquid ascends and descends multiple times before erupting. Once the dike erupts, a significant proportion of its volume is expelled, converging toward the vent.

Albert et al. (2020) demonstrated a similar result in a basaltic dike, through the crystal growth patterns associated with monogenetic eruptions. They analyzed the olivine crystals from Parícutin and showed that they formed in a dynamic environment. Crystals from the initial, propagating phase of the eruption have a variety of zoning patterns, sometimes oscillatory zoning, which grew on the timescale of dike propagation. These zoning patterns

Writing – original draft: Stephen Pansino
Writing – review & editing: Stephen Pansino, Adel Emadzadeh, Benoit Taisne

indicate that the crystals were exposed to a range of temperatures, pressures, and oxygen fugacities, and cycled between such conditions. By contrast, crystals representing the later stages of the eruption have simpler growth patterns and are entirely characterized by normally zoned olivines, which ascend directly from their source to the surface. This evidence suggests that the dike had an initial, complex phase of propagation, followed by a period that was characterized by simple ascending flow.

Crystal textures do not always show a record of circulation. A dike's propagation can be faster than the timescale of crystal growth. In this case, the propagation phase of monogenetic eruptions is not well recorded in the crystal textures and is only evidenced in the number of microlites (Coote et al., 2018; Schonwalder-Angel et al., 2018). When larger, oscillatory-zoned crystals are found, their texture does not necessarily indicate circulation. They have been interpreted to be formed by repeated recharge events, or possibly due to the progressive degassing and cooling of magma (Crabtree & Waters, 2017; Gordeychik et al., 2018).

The objective of this study is an experimental investigation into the conditions which lead to circulation in a propagating dike. We hypothesize that the form of magma flow is controlled by the forces acting on the dike (e.g., buoyancy, source pressure, fracture pressure) and test this through analogue experiments of varying liquid fluxes and rheologies. We then discuss the results in the context of crystal zoning patterns.

2. Methods

2.1. Experimental Setup

We conducted a series of eight scaled laboratory experiments (Table 1) with solid gelatin as the crust analogue and different fluids (water, liquid gelatin and vegetable oil) as the magma analogue. We label isothermal experiments, with water or vegetable oil, as the “C” series and thermal, solidification-prone experiments, with liquid gelatin, as the “S” series (Table 1). Water and oil are Newtonian liquids, while the liquid gelatin seems to have a temperature-dependent, shear-independent viscosity, as described by Pansino and Taisne (2019) and Pansino et al. (2019).

We prepared each gelatin medium following common practice (e.g., Kavanagh et al., 2013; Menand & Tait, 2002; Pansino & Taisne, 2019), by dissolving 3 to 3.5 wt% of granular gelatin in 112 L of deionized water heated to 60°C. We poured the gelatin into a 50 × 50 × 50 cm³ tank and covered it with a layer of oil to prevent evaporation and the formation of a hard skin at the surface. Finally, we placed the tank into a cold room to solidify at 15°C for 3 days. We performed the experiments inside this cold room, which offers good control of lighting conditions and prevents any warming of the gelatin. For two of the S series experiments, we added 5 wt% concentration of white sugar to the solution to increase its density. Using this concentration of sugar increases its density and exerts buoyancy force on the dike, without significantly changing the rheology; Choi et al. (2004) found gelatin becomes a viscous material at concentrations exceeding 30 wt% of sucrose.

Before performing each experiment, we estimate the gelatin's Young's modulus by recording the shear wave velocity, which are visible using polarizing filters, using the method described by Pansino and Taisne (2020). Shear wave velocity, v_s , is related to the shear modulus, G , via $G = \rho v_s^2$ (Table 3), for a solid medium with density, ρ (Lee et al., 2017). The Young's modulus is related to the G and the Poisson's ratio, ν , via $E = 2G(1 + \nu)$. We assume gelatin is an incompressible material with ν of 0.5. Pansino and Taisne (2020) found through analysis of shear and pressure waves that gelatin has a ν of at least 0.47, but concluded it is likely higher, approaching 0.5. The medium's resistance to fracture is characterized by the fracture toughness parameter, K_c , which depends on E and surface energy, γ , where $K_c = (2\gamma E)^{1/2}$ (Menand & Tait, 2002). We assume gelatin has γ of 1 J/m² (Kavanagh et al., 2013; Menand & Tait, 2002). Smittarello et al. (2021) found that the surface energy is marginally affected by the addition of salt (by less than a factor of 2), but to the best of our knowledge, the effect of sugar on surface energy has not been rigorously examined. We assume it has a negligible effect on surface energy and that variation in fracture toughness is primarily a function of E . Errors are approximately $\pm 10\%$ of E measurements (Table 1) and are specified in more detail in Supporting Information S1.

We injected the liquid via two different methods. For most experiments (in both the S and C series), we injected the liquid at a constant volumetric flux using a peristaltic pump (Figure 1; see Table 1, “pump” driven experiments). In this case, the dike volume at any time can be estimated using the flux rate. For experiments C4 and C5, we adjusted the setup to be gravity-driven, in which we placed a beaker with liquid surface 1.25 m above

Table 1
Experimental Conditions

Exp	C_{gel} (wt%)	C_{sug} (wt%)	E (Pa)	K_c (Pa · m ^{1/2})	Liquid	$\Delta\rho$ (kg/m ³)	μ (Pa · s)	Q (mL/min)	DM	L_b (cm)
C1	3.0	0.0	3,620	85	Veg. oil	100	10 ⁻¹	11	Pump	19.6
C2	3.0	0.0	3,520	84	Veg. oil	100	10 ⁻¹	170	Pump	19.4
C3	3.0	0.0	1,790 ^a	60	Veg. oil	100	10 ⁻¹	2	Pump	15.5
C4	3.0	0.0	1,420 ^a	53	Veg. oil	100	10 ⁻¹	21	Gravity	14.4
C5	3.5	0.0	1,840 ^a	61	Water	10	10 ⁻³	15–350 ^b	Gravity	72.6
S1	3.5	5.0	3,990	89	Gelatin	70	10 ⁻²	38	Pump	25.7
S2	3.5	5.0	4,580	96	Gelatin	70	10 ⁻²	38	Pump	26.9
S3	2.7	0.0	2,400 ^c	69 ^c	Gelatin	10	10 ⁻²	3	Pump	79.4

Note. The symbols represent gelatin concentration (C_{gel}), sugar concentration (C_{sug}), Young's modulus (E), fracture toughness (K_c), density contrast ($\Delta\rho$), viscosity (μ), volumetric influx (Q), and driving method (DM). The experiment names are labeled with "C" for isothermal experiments and "S" for those that are temperature-dependent and prone to solidification.

^aHere the filters on our water purifier began to expire, leading to a decrease in E (gelatin is a fickle material). We increased the concentration of C5, relative to the other C experiments, to offset this trend. Subsequent experiments, not reported in this study, after replacing the filters had higher E of 2,800–3,200 Pa at 3.0 wt%, indicating the filters were the main cause of this trend. ^bThe flux variation in C5 is due to the gravity-driven setup (see Figure 1a). Water was allowed to flow from an elevated beaker at a variable flux. By contrast, we had a gravity-driven experiment of oil, which had an extremely stable flux, because of its viscosity. ^cNo measurement. Estimated roughly using the final strength measurements of other gelatins presented in Pansino and Taisne (2020), following the relationship $E = 2750C_{\text{gel}} - 5,000 = 2,425$ Pa, which we round off to 2,400 Pa, as this is just an estimate. Note this experiment was prepared before the filters began to expire.

the gelatin surface and allowed gravity to drive it into the gelatin (Figure 1a). We placed the beaker on a scale to measure a time series of mass loss, which allowed us to record the dike volume (mass divided by density) and flux rate (differential of volume with respect to time). The driving pressure was nearly constant, since the liquid surface dropped by less than 1 cm during the experiment, corresponding to a total pressure decrease of less than 1%. Note, further details about the gelatin, liquids and experimental setup are given in Supporting Information S1.

For the thermally dependent S series experiments, the injected liquid gelatin was kept warm using a thermal bath. We placed a thermocouple in a basal supply reservoir (red object illustrated in Figure 1, attached to the tank bottom) to monitor its temperature (Figure 1) and we attempted to maintain a target temperature of 32°C. This temperature is slightly above the gelatin liquidus (~28°C) and therefore scales to the injection temperature for basaltic dikes (Delaney & Pollard, 1982; Pansino et al., 2019; Taisne & Tait, 2011).

2.2. Flow Visualization Using Particle Image Velocimetry

The liquid flow field within the dike was measured using 2D PIV, which statistically estimates the liquid velocity field inside a rectangular grid, using cross-correlation of pairs of images (Adrian, 1991; Raffel et al., 2013; Schroeder & Willert, 2008; Zhang & Porfiri, 2019). The particle concentration needs to be such that the pattern matching can recognize the displacement of individual groups of particles in each observation window. We gradually increased the particle concentration between experiments from ~1 to ~5 g/L, to improve the quality of PIV measurements (note C1 has somewhat noisy measurements due to its low particle concentration). Particle concentrations for each experiment are specified in Supporting Information S1.

The flow was seeded with passive Pliolite tracer particles (0.8–1.0 mm in diameter, 1,030 kg/m³ density, 1.558 refractivity index), which faithfully follow the motion of the fluid and act as a proxy to measure the velocity field. The particles are larger than typically used in PIV studies (e.g., Kavanagh et al., 2018; Zhang & Porfiri, 2019), to compensate for the light scattering due to the gelatin medium and our relatively weak light source. We note that, depending on the liquid density and viscosity, the particles have a calculated Stokes settling velocity of 3.0–7.3 mm/s (water), 0.20–0.49 mm/s (gelatin), or 0.13–0.32 mm/s (vegetable oil), which can be similar in magnitude to the experimental velocities. However, it is likely that the smallest particles preferentially entered the dike, since these were the least likely to settle in the much-wider basal reservoir, below the main tank. Moreover,

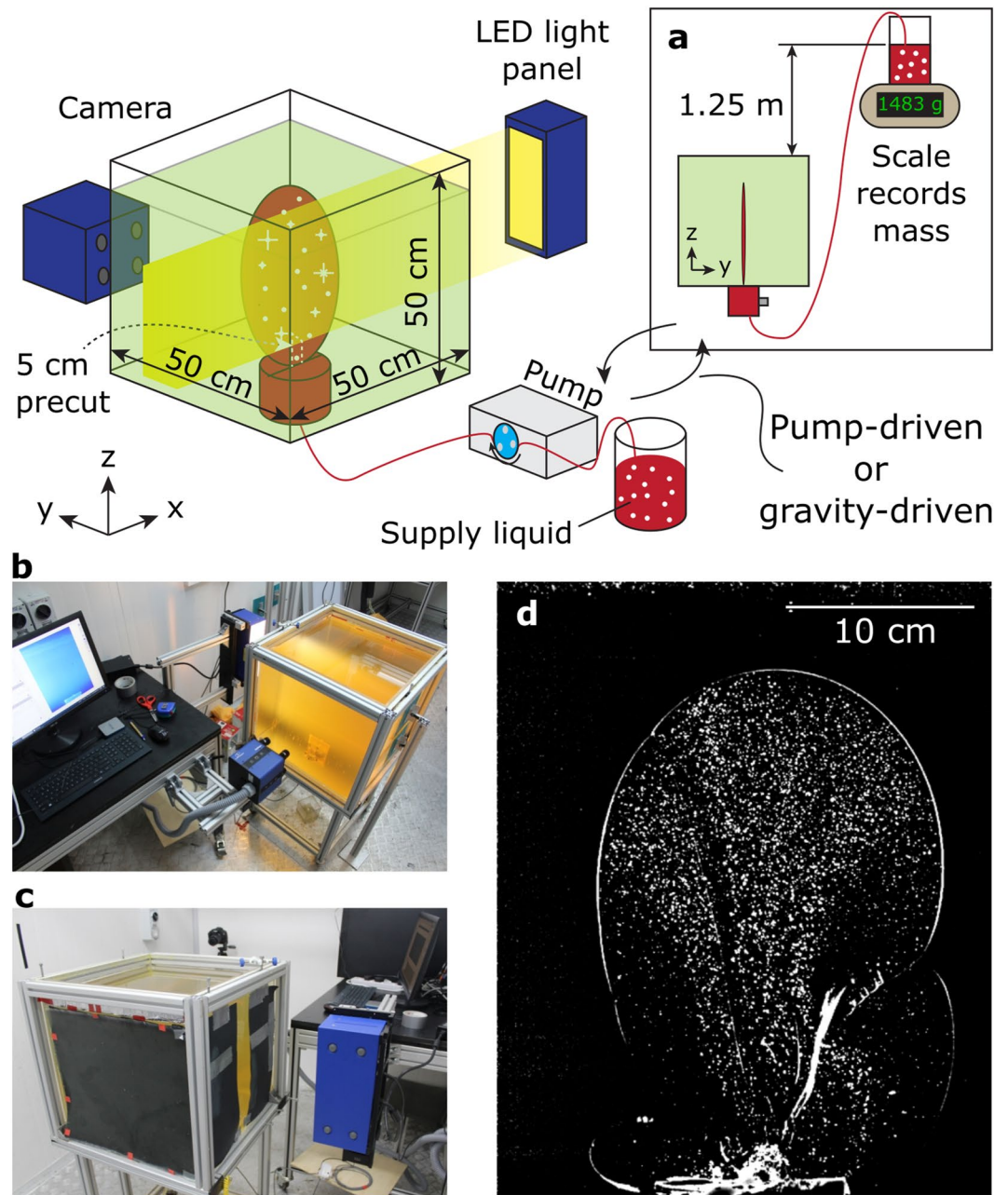


Figure 1. A schematic of the experimental setup. The magma analogue (here shown in red for visibility) is seeded with tracer particles and injected into a solid gelatin medium. The particles are illuminated by an LED light panel that lights a volume of the gelatin, maintaining illumination even if the dike is not perfectly vertical (not the case for more-common laser sheets). Liquid is injected at a constant flux using a peristaltic pump. (a) Alternatively, we use a gravity-driven setup to attempt to supply a constant pressure and variable flux. In this scenario, we record a mass time series to be converted to volume and volumetric flux. (b) A photo of the visualization setup, taken from the front of the tank. Light enters the left side of the tank and is reflected by mirrors on the right. The cameras are positioned in front of the tank. The software package that controls the setup can be seen operating on the computer. (c) A photo taken from the back. Black paper prevents light from entering, illuminating only a narrow band where the dike is expected to propagate. (d) A pre-processed image from experiment C2, in which an initial reference image is subtracted from the current image, to highlight the particles within the dike. Note this experiment displays two small, en-echelon dikes, which were quickly overcome by the main dike and ceased propagation.

once particles enter the dike, the settling estimate is no longer valid as the particles are in a confined dike, not an infinite liquid medium. We performed settling velocity measurements in a dike of liquid gelatin, by turning off the pump mid-propagation and allowing the flow to come to rest, which indicates settling velocities less than

0.05 mm/s (see Supporting Information S1). Assuming this measurement is proportional to the liquid density and inversely proportional to viscosity, then the revised settling velocity is less than 0.03 mm/s for vegetable oil and 0.75 mm/s for water, about an order of magnitude less than predicted by the Stokes settling velocity. The slowest experiments (C3, S3) have maximum flow velocities that are faster by a factor of 1–3 times, whereas the other experiments are faster by a factor of 9–410 times. However even for the slowest experiments, we observe that particles appear to travel in a way that qualitatively follows the fluid flow with negligible settling (e.g., in S3 flowing in arcs that match the penny-shaped curvature of the dike), which leads us to believe the true settling velocity is even lower than we estimate.

The visualization setup consists of a 300W LED illumination source, a set of four high-speed cameras (Mini-shaker *L*, product of LaVision, www.lavision.de), a synchronization board and a computer with a dedicated software package, DaVis 10, which can measure the fluid velocity in a $300 \times 100 \text{ mm}^2$ cross section of the experiment. This LED light source is weaker than more-common laser sheets, but has the advantage of illuminating a volume, so particles are visible even if the dike propagates at a slight angle (their exact orientation is challenging to control and can therefore be difficult to align with a laser sheet). When combined with the four high-speed cameras, the system enables 3D tomographic PIV measurements, under the right conditions. However, we found that light distortion between the injected liquid and the gelatin medium potentially inhibits 3D measurements, which is pronounced when the liquid has very different optical qualities from gelatin; such is the case for vegetable oil and, to a lesser degree, water. For simplicity and uniformity, we present 2D PIV results, performed on the recording from a single camera, which requires no 3D calibration.

As mentioned, gelatin scatters light and therefore the intensity of light decreases from the side nearest to the LED light source to the opposite end. To overcome this issue, we placed small mirrors on the opposing side of the tank to reflect the light back to the observation area, which improves the light homogeneity. The tank wall nearest to the LED was also partly covered with opaque, black paper, to let the light shine through a relatively narrow gap (5–10 cm) into the gelatin and diminish the light pollution due to scattering outside of the region of interest. Further details of the visualization system are given in Supporting Information S1.

2.3. Scaling

Dike propagation in a homogeneous medium is driven by a combination of buoyancy, P_b , and source reservoir overpressure, ΔP . It is resisted by the fracture pressure at the dike tip, P_f , elastic pressure in the medium, P_e , and viscous pressure drop in the liquid, P_v . Each of these (except the source pressure) are typically quantified by relationships that are dependent on the dike's geometry (Lister, 1990; Lister & Kerr, 1991; Taisne et al., 2011):

$$P_b \sim \Delta \rho g L, \quad (1)$$

$$P_f \sim \frac{K_c}{\min(L, B)^{1/2}}, \quad (2)$$

$$P_e \sim \frac{GH}{\min(L, B)(1 - \nu)}, \quad (3)$$

and

$$P_v \sim \frac{12\mu v_l L}{H^2} \sim \frac{12\mu QL}{BH^3}. \quad (4)$$

In the above equations, we define the dike dimensions as the vertical length, L , the horizontal breadth (transverse dimension of propagation), B , and the opening thickness, H . The symbol $\Delta \rho$ is the liquid-medium density contrast, g is the gravitational acceleration, μ is the viscosity, Q is the volumetric flux and v_l is the liquid's characteristic velocity scale, $v_l = Q/(BH)$. The denominators of Equations 2 and 3 use the smaller of the L and B dimensions (not both values), which we assume characterizes the magnitude of their respective stresses, following Taisne et al. (2011). The factor of 12 in the P_v equation is a constant that arises when deriving the equation for a simple Poiseuille flow in a slot geometry (e.g., Jones & Llewellyn, 2021; Whitehead & Helfrich, 1991).

As a dike grows, the pressure balance can evolve, so that the dominant pressures can vary with time. For example, the ΔP is the dominant driving force when the dike is small, whereas the P_b can become significant as the dike

grows in length. For the resisting forces, the P_f is initially large and becomes smaller as the dike grows. The P_e and P_v are dependent on the thickness, H , and either the length, L , or breadth, B (whichever is smaller). For dikes that become thinner as they grow, the P_e starts large and decreases as the dike grows. The P_v , by contrast, increases as the dike becomes longer and/or thinner, but in gelatin is negligibly small (Menand & Tait, 2002).

The dike is characterized as “small” or “large” via the buoyancy length, L_b , the length at which the dike is buoyancy enough to propagate without additional pressure. This occurs when $P_b \sim P_f$ (Menand & Tait, 2002), which yields the relationship,

$$L_b \sim \left(\frac{K_c}{\Delta \rho g} \right)^{2/3}. \quad (5)$$

The relative length, L^* , can therefore be defined as,

$$L^* = \frac{L}{L_b}. \quad (6)$$

Before the dike reaches the buoyancy length, it maintains a circular penny-shape and afterward it begins to become vertically elongated (Menand & Tait, 2002). The propagation then becomes driven by the upper head of the dike, which is roughly penny-shaped, as has been observed by Taisne et al. (2011). If we assume a penny-shaped head, then the buoyancy pressure can be redefined as,

$$P_b = \Delta \rho g B. \quad (7)$$

In the lower, thinner tail by contrast, buoyancy balances with viscous forces and therefore does not contribute to propagation (Taisne et al., 2011).

According to this framework, we therefore define the pressure ratio, Π_p , to determine the buoyancy pressure's relative magnitude:

$$\Pi_p = \frac{P_b}{P_f} = \frac{\Delta \rho g B^{3/2}}{K_c} = \left(\frac{B}{L_b} \right)^{3/2}. \quad (8)$$

Note that, for a constant-volume dike, with no influx, the penny-shaped head does not significantly grow in length, so Π_p remains nearly constant. If there is an influx, the dike head may enlarge, causing Π_p to increase. We argue that the Π_p parameter effectively quantifies the ratio of buoyancy pressure to total driving pressure (source pressure, ΔP , plus buoyancy). This is because the total driving pressure in gelatin experiments will always be in balance with both the elastic and fracture pressures in the dike head (Menand & Tait, 2002; Pansino et al., 2022), so that $P_b + \Delta P \sim P_e \sim P_f$. By extension, as P_b increases and comes into balance with P_f , ΔP decreases accordingly. Following this assumption, ΔP becomes negligible when $L^* > 1$, though in practice, only some of our experiments reach negligible ΔP : C2 and C4 have a minimum $\Delta P/P_b \sim 0.1$; C1, S1 and S2 have $\Delta P/P_b \sim 0.3$; C3 has $\Delta P/P_b \sim 0.7$; C5 and S3 have $\Delta P/P_b > 1$.

The liquid flow within the dike is governed by the Reynolds number, Re , which is a ratio between inertial forces, defined as $\rho v^2/L$, and the viscous forces, defined as $\mu v/H^2$ (Schlichting & Gersten, 2017), so that $Re = \rho v H^2/(\mu L)$. For characteristic velocity $v \sim Q/HB$, Re can be expressed as,

$$Re = \frac{\rho Q H}{\mu L B}. \quad (9)$$

Since the experiments are thin with a low influx, the liquid generally remains in the laminar regime, with $Re \ll 1$.

The solidification-prone, S series experiments have additional thermal scaling. The dimensionless thermal flux, Φ , is a ratio of heat advection to heat loss due to conduction,

$$\Phi = \frac{QH}{\alpha LB}, \quad (10)$$

(Taisne & Tait, 2011) where α is the thermal diffusivity, which for gelatin is $7.4 \times 10^{-8} \text{ m}^2/\text{s}$ (Pansino et al., 2019). It is related to Re via the Prandtl number, Pr , so that $Pr = \mu/(\alpha \rho)$ and $\Phi \sim RePr$. When $\Phi \gg 1$, heat loss due

Table 2
Comparison of Experimental and Natural Basaltic Dikes

Parameter	Experiments	Nature
L (m)	0.05 to 0.34	10^1 ^a to 10^4 ^a
B (m)	0.05 to 0.25	10^1 to 10^4 ^a
H (m)	0.003 to 0.012	1 to 10 ^b
ρ (kg/m ³)	910 to 1,000	2,600 ^c
$\Delta\rho$ (kg/m ³)	10^1 to 10^2	10^1 to 10^2 ^c
μ (Pa · s)	10^{-3} to 10^{-1}	10^2 to 10^4 ^b
G (Pa)	470 to 1,530	30×10^9
K_c (Pa · m ^{1/2})	53 to 96	10^6 ^d
Q (m ³ /s)	0.03 to 2.8×10^{-6}	1 to 100 ^e
α (m ² /s)	7.4×10^{-8}	10^{-6} ^f
L_b (m)	0.14 to 0.79	100 to 470
L^*	0.13 to 2.20	10^{-2} to 10^2
Π_p	0.06 to 1.11	10^{-2} to 10^0
Re	10^{-4} to 10^0	10^{-10} to 10^2
Φ	10^{-2} to 10^3	10^{-6} to 10^8
Θ	0.11	0.05 to 0.10

Note. Lower estimates in experiments and nature given to estimate dimensionless numbers when the dike is small.

^aAssuming a range of sizes. ^bWada (1994). ^cTaisne and Jaupart (2009). ^dMeredith and Atkinson (1985). ^eTraversa et al. (2010). ^fDouglas et al. (2016).

3. Results

3.1. Qualitative Observations

For experiments done with oil (experiments C1 through C4; Table 1), the flow pattern evolved as the dikes grew. They showed an initial circulation when small (Figure 2i), which was accompanied by radial, penny-shaped, growth. As the dikes grew, they became vertically elongated and the circulation ceased, transitioning to upward flow (Figures 2ii and 2iii). Though the flux varied over two orders of magnitude, the propagation and overall flow pattern varied little between experiments. When the dikes erupted, they began with an initial rapid expulsion of the liquid from the fracture, due to the release of elastic pressure, followed by a steady-state ascending flow pattern, from source to surface (Figures 2iv and 2v).

When we injected water, we made similar observations to a previous study (Kavanagh et al., 2018), in which the dike displayed a strong circulation throughout the entire propagation (Figures 2vi to 2viii). This took the form of a constrained upward flow region with downward return flow along the lateral margins. The experiment was gravity-driven to ensure a constant, hydrostatic pressure at the entrance of the basal reservoir. The large range of fluxes, from 15 to 350 mL/min, is primarily associated with some experimental difficulty, in which the supply tubing clogged midway through the experiment, which we had to shake to release. This restricted the influx and stopped the propagation, effectively pausing the experiment and allowing the analysis of only the beginning 10% and final 15% of the experimental time series. When the dike erupted, it displayed a similar flow evolution to the other C series experiments (Figures 2ix and 2x). We observed other similar flow behaviors described by Kavanagh et al. (2018), such as instabilities in the upward jet and bifurcation of the basal part of the jet, which was most apparent when the dike was small. The C series experiments suggest that there is buoyancy control on circulation and that the flux is less important, as the high-flux C2 ($Q = 170$ mL/min) has a similar flow evolution to the lower-flux C1, C3, and C4 experiments ($2 \leq Q \leq 21$ mL/min).

to conduction dominates the system, and when $\Phi \gg 1$, advection dominates. The dimensionless temperature, Θ , indicates how hot the initial liquid temperature, T_0 , is, in comparison with its liquidus temperature, T_l , and the ambient temperature, T_a ,

$$\Theta = \frac{T_0 - T_l}{T_0 - T_a}. \quad (11)$$

Θ approaches 0 when T_0 approaches T_l . Delaney and Pollard (1982) argue that magma is likely injected near the liquidus temperature, so that $0.05 < \Theta < 0.10$. For our experiments, gelatin has $T_l = 30^\circ\text{C}$ and the ambient condition was $T_a \sim 15^\circ\text{C}$, so we choose $T_0 \sim 32^\circ\text{C}$, which corresponds to $\Theta \sim 0.11$.

Our analogue experiments are scaled with natural conditions for basaltic dikes, via the dimensionless parameters, L^* , Π_p , Re, Φ , and Θ , some which change as the dike grows. Table 2 shows typical values for basaltic magma properties and dike geometries in nature, as well as their analogs in our experiments. There is good overlap for Π_p and Re between experiments and natural systems, and both are generally defined by laminar flow, so $\text{Re} \ll 1$. The L^* overlaps on the lower end for magmatic systems, mainly due to their size proportions. Magmatic dikes reach their buoyancy length when they grow to several hundreds of meters in length, but may continue to propagate for kilometers. In our experimental setting, the buoyancy length for oil dikes is half the size of our tank, therefore $L^* \leq 2$. For water dikes, the buoyancy length is greater than the size of our tank and therefore models small or non-buoyant dikes ($L^* \approx 0.6$). The thermal flux parameter similarly has a narrower range in experiments than nature, but in both cases displays conduction dominated $\Phi \ll 1$ and advection dominated $\Phi \gg 1$ flow. The dimensionless temperature was chosen to match nature, so that $\Theta \sim 0.1$.

Table 3
Meanings of Symbols Used in This Document

Symbol	Units	Meaning
Material properties		
$\Delta\rho$	kg/m ³	Liquid—medium density contrast
ρ	kg/m ³	Density
μ	Pa · s	Dynamic viscosity
G	Pa	Shear modulus
E	Pa	Young's modulus
ν	–	Poisson's ratio
γ	J/m ²	Surface energy
K_c	Pa · m ^{1/2}	Fracture toughness
Dike dimensions		
L	M	Length (vertical)
L_b	M	Buoyancy length scale
L_v	M	Viscous length scale
B	M	Breadth (horizontal)
H	M	Opening thickness
Kinetic terms		
u	m/s	Horizontal velocity
v	m/s	Vertical velocity
\mathbf{v}	m/s	Velocity vector
v_s	m/s	Shear wave velocity
v_1	m/s	Characteristic velocity
v_{\max}	m/s	Maximum vertical velocity
v_{\min}	m/s	Minimum vertical velocity
v_{\inf}	m/s	Influx velocity scale
v_{lub}	m/s	Lubrication theory velocity scale
\bar{v}	–	Overline indicates mean
\bar{v}_{med}	–	Overline + med indicates median
σ	m/s	Median absolute deviation of vertical velocity
Q	m ³ /s	Volumetric flux
Q_a	m ³ /s	Ascending flux
Q_d	m ³ /s	Descending flux
g	m ² /s	Gravitational acceleration
Pressure terms		
ΔP	Pa	Driving source pressure
P_b	Pa	Buoyancy pressure; $P_b = \Delta\rho g B$
P_f	Pa	Fracture pressure; $P_f = K_c/B^{1/2}$
P_e	Pa	Elastic pressure; $P_e = GH/B(1 - \nu)$
P_v	Pa	Viscous pressure drop; $P_v = \mu QL/(BH^3)$
Thermal terms		
α	m ² /s	Thermal diffusivity
T_0	°C	Initial temperature
T_1	°C	Liquidus
T_a	°C	Ambient temperature

The S series experiments represent a variation on the C series, so that the liquid is prone to solidification. For experiments S1 and S2, the magma analogue was buoyant and the dike geometry evolved in a similar way to the experiments made with oil, in which the dike gradually elongated in the vertical direction. However, thermal effects modified the internal flow field. Some combination of solidification and viscosity variations (due to temperature) encouraged flow near the thicker, warmer, central region (Figure 2, xi to ;xiii), and the circulating pattern became confined to the upper head of the dike, persisting throughout the experiments. The lower, lateral edges of the dike tail show markedly lower velocities, as solidification presumably dominated the region. Between these solid regions, a localized, high-velocity conduit of liquid connected the source to the dike head. Experiment S3, which was not buoyant, evolved in a similar way to experiment C5, made with water. It maintained circulation throughout the entire propagation and similarly maintained a penny-shaped form with radial growth. Solidification constrained the flow to a lesser degree than S1 and S2 and was most evident just before eruption.

The eruptions in the S series were similar to the C series and began with an initial expulsion of the liquid (Figures 2xiv and 2xv). This evacuated liquid from the still-molten dike head, while the partially solidified tail showed little to no flow. The flow then evolved into a steady-state, unidirectional flow along the dike's central axis, which was comparatively narrower than the C series due to solidification. As described by Pansino et al. (2019), solidification eventually restricts the upward flow in a sub-cylindrical conduit, in which advective heat flux balances with conductive heat loss.

We briefly note here that boundary conditions did not influence our experiments, even for the largest dikes. Since dikes generate their own local stress field, boundary conditions only come into effect in the presence of a large external stress (Watanabe et al., 2002). This can be a large far field stress (e.g., gelatin is incompressible, so a large dike generates a compressive stress field throughout the medium) or when the tip is significantly close to an interface. As we show in a previous publication (Pansino et al., 2022), which uses data from the C series experiments presented here, the far field stresses are always at least an order of magnitude lower than the dikes' internal stresses. Near-field stresses ahead of a dike tip are assumed to be negligible following results from Rivalta and Dahm (2006), who show that constant-volume dikes accelerate as they approach a free surface, when the distance of the tip is similar to the dike's half-length. Assuming this rule of thumb also applies to dikes approaching the tank wall, the half-breadth in our experiments always remained larger than the distance to the wall. This agrees with our previously published results, which indicate that the horizontal propagation rate in these experiments depends only on the buoyancy, driving pressure and volumetric influx, with no influence from an external stress source.

We also note that later images from experiment C1 ($L^* > 0.92$) have noisy-appearing results on the right half of the dike (e.g., Figure 2iii-v), which occurs primarily due to low particle concentrations. A secondary factor is light transmission, in which oil reflects light, causing a shadow to be cast on the right side of the dike. This causes the results on the left side of the dike (better lit) to be less noisy than the right. We did not notice this asymmetry with other oil dikes that have greater particle concentrations. To mitigate this issue for statistical analysis, we crop the right side of the dike. For experiment S3, the camera was partially misaligned, causing the dike to grow out of frame, so we similarly only analyzed half of the dike.

Table 3
Continued

Symbol	Units	Meaning
Dimensionless terms		
L^*	–	Dimensionless length; L/L_b
Π_p	–	Dimensionless buoyancy force; $\Pi_p = P_b/P_t = \Delta\rho g B^3/2K_c$
Re	–	Reynolds number; $Re = \rho QH/(\mu BL)$
Φ	–	Dimensionless thermal flux; $\Phi = QH/(\alpha LB)$
Θ	–	Dimensionless temperature; $\Theta = (T_0 - T_1)/(T_0 - T_a)$
Pr	–	Prandtl number; $Pr = \mu/(\alpha\rho)$
Π_Q	–	Dimensionless liquid exchange; $\Pi_Q = Q_d /Q_a$

We quantify the vertical velocity distribution using cumulative density functions (Figure 3). The shape of the distribution changes primarily with buoyancy, so that non-buoyant, source-pressure-dominated dikes (with low L^*) have a clear downward (negative v) component, which disappears as buoyancy becomes significant ($L^* \rightarrow 1$, visible in Figures 3c, 3e, and 3h; less visible in Figures 3a and 3g due to higher maximum velocity). The upward velocity also evolves with buoyancy. Non-buoyant dikes show a decrease in the upward velocity, as the velocity field decelerates inside a radially growing dike. However, as buoyancy becomes significant, the upward velocity increases again (visible in Figures 3a, 3b, and 3d). The median absolute deviation, σ , and median vertical velocity, \bar{v}_{med} , respectively quantify the variation and magnitude of the flow field and represent the slope and position of the CDF. The relative variation σ/\bar{v}_{med} drops as buoyancy increases (Figure 3j).

3.2. Controls on Liquid Flow Velocity

To be able to characterize the flow, we compare the median magnitudes of liquid velocity, \bar{v}_{med} , (over the entire velocity field for any given time step) with two velocity models. The first is the superficial influx velocity, v_{inf} ,

$$v_{inf} = \frac{Q}{\pi H \sqrt{2[(L/2)^2 + (B/2)^2]}} \quad (12)$$

in which the influx flows from the source toward the edge of the crack, which has an elliptical shape with perimeter, $\pi\{2[(L/2)^2 + (B/2)^2]\}^{1/2}$ (i.e., flux divided by the cross-sectional area, where the area is an arcing surface following the perimeter, defined as $\pi H\{2[(L/2)^2 + (B/2)^2]\}^{1/2}$). This model best-fits the data when the buoyancy is relatively small in comparison to the fracture pressure, so $\Pi_p \ll 1$ (Figure 4).

The second velocity model is described by lubrication theory, v_{lub} ,

$$v_{lub} = \left(\frac{\Delta\rho g Q^2}{12\mu B^2} \right)^{1/3}, \quad (13)$$

(Roper & Lister, 2007; their Equation 2.4). Note this is for a 2D dike with a 2D flux parameter; we have adjusted it to average the 3D influx over the breadth of the dike (i.e., $Q_{2D} \sim Q/B$). This model is defined for a vertically growing dike with dominant viscous pressure drop and negligible fracture pressure. We observe it fits better with experimental data when $\Pi_p \geq 1$ (Figure 4), which coincides with an ascending flow pattern (e.g., Figure 2iii). Overall, we observe the data transition between the two models, as the buoyancy becomes the dominant driving force. Note we do not discuss S series data at the moment, as solidification affects the flow field.

The horizontal and vertical components of flow velocity, respectively u and v , also depend on Π_p . By assessing the mean value of $|u|$ (absolute value, so that leftward and rightward flow are treated equally), against the mean value of the velocity vector, $|\bar{u}|/\bar{v}$, the horizontal component diminishes as buoyancy increases (Figure 5a). This is evident for the isothermal C series experiments, but not for S series experiments, which as stated in Section 3.1 do not appear to evolve in flow pattern with time. We can see corresponding results for the vertical component, \bar{v}/\bar{v} , of C series experiments, in that \bar{v}/\bar{v} approaches 1 as Π_p approaches 1 (Figure 5b). For the S series, this does not appear to evolve much with growth.

3.3. Vorticity

We evaluate the effect of flow vorticity, ω , on the overall flow pattern. For a planar dike, with a quasi-2D flow field, vorticity is defined via the vertical and horizontal velocity gradient across a pixel,

$$\omega = \partial v/\partial x - \partial u/\partial y. \quad (14)$$

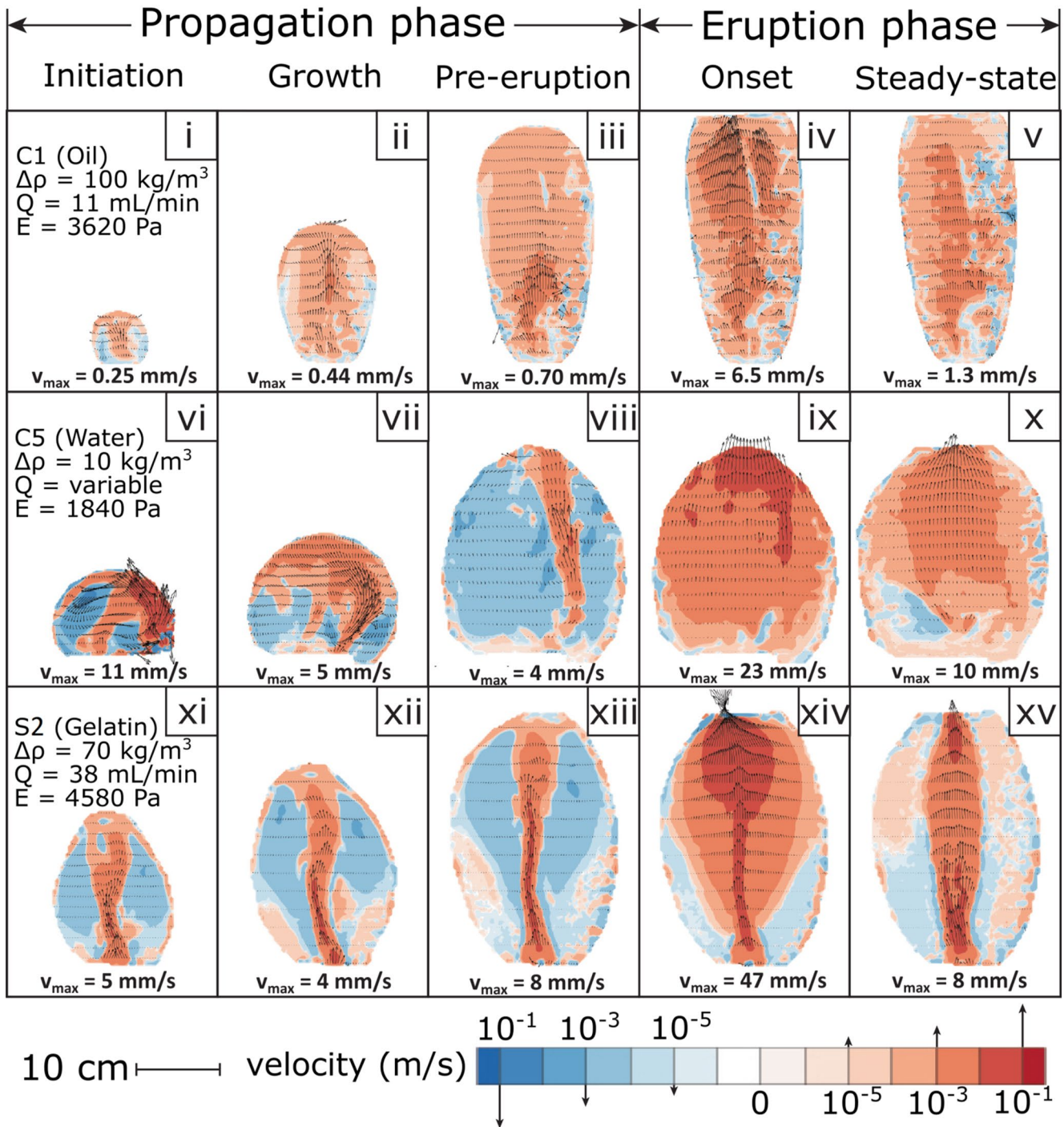


Figure 2. Contrasting flow evolution between oil-, water-, and gelatin-filled dikes (respectively experiments C1, C5, and S2). Color represents the vertical component of velocity (on a log scale), in which red and blue respectively correspond to upward and downward velocity. Vectors indicate the flow field profiles. All dikes displayed internal circulation when small (i, vi, xi), while only weakly-buoyant and solidification-prone dikes maintained it when larger (viii, xiii). Oil-filled dikes transitioned to a simple ascending flow profile as they grew (iii). At the onset of eruption, all dikes display a rapid expulsion of liquid onto the surface (iv, ix, xiv), followed by a steady flux (v, x, xv). For solidification prone liquid, a proto-conduit forms (xv) along the path of the upward flow (xi–xiii).

The mean of the absolute value of vorticity (we do not distinguish between clockwise and counterclockwise rotation), $|\overline{\omega}|$, depends on the maximum and minimum vertical velocities (or in cases with return flow, the maximum downward velocity), respectively v_{max} and v_{min} , and the transverse dimension that confines the swirling motion of

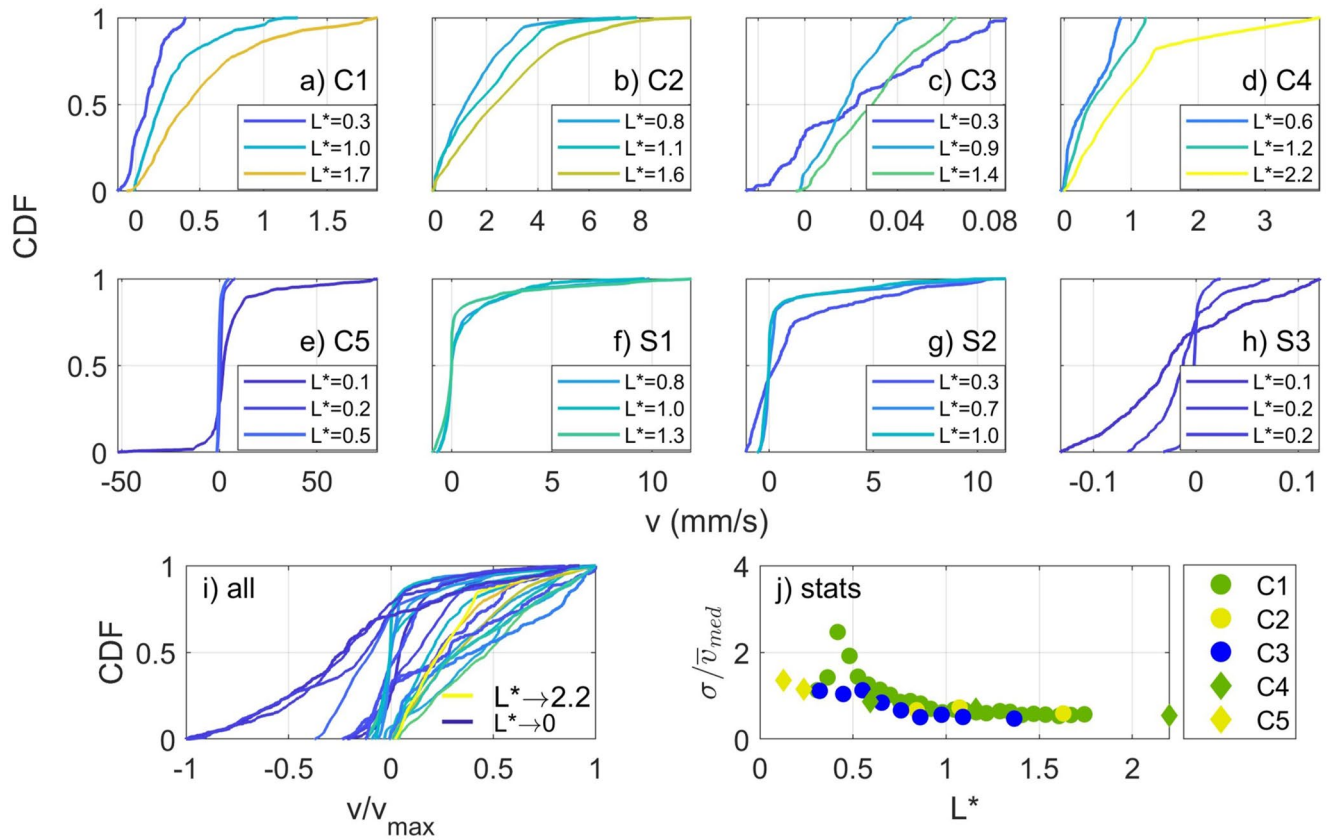


Figure 3. (a–h) Cumulative density functions (CDF) of the vertical velocity (from the 1st percentile to 99th percentile), for each experiment. Each plot has three curves, representing the first, last, and a middle measurement. The corresponding dimensionless sizes, L^* , are given and correspond to color, with blue and yellow respectively representing low and high values of L^* . (i) A plot showing each of the curves normalized to its 99th percentile value (approximately the maximum velocity). Colors are as in the previous plots. Downward velocity is negligible for dikes with $L^* > 1$. (j) The median absolute deviation, normalized by the median vertical velocity, shown against L^* . The deviation is relatively high when $L^* < 1$, indicating a circulating flow pattern. Colors represent qualitative flux (blue is low, green is moderate, yellow is high) and symbols represent the injection method (circles are pump-driven, diamonds are gravity-driven). S experiments are not included here as circulation continues for $L^* > 1$, indicating some other control on circulation than buoyancy.

the flow, in our case B (Figure 6a). Experiments show a 1:1 correlation for $|\overline{\omega}|:2(v_{max}-v_{min})/B$. This is sensible, since, for a dominantly vertical flow field,

$$\begin{aligned} |\overline{\omega}| &\sim \frac{2}{B} \int_0^{B/2} \omega dx \\ &\approx \frac{2}{B} \int_0^{B/2} \left(\frac{\partial v}{\partial x} \right) dx \\ &\approx 2[v(x=0) - v(x=B/2)]/B, \end{aligned} \quad (15)$$

for a dike centered at $x=0$, with edges at $x=-B/2$ and $B/2$. The v_{max} and v_{min} respectively tend to occur near $x=0$ and $|x|=B/2$, and therefore lead to this strong correlation. By comparing the vorticity with Π_p , we could not find a consistent relationship evident in every experiment (Figure 6b; data generally has weak positive or negative correlation). If we make a dimensionless parameter, Π_ω , that scales the vorticity to the velocity and dike size,

$$\Pi_\omega = \frac{|\overline{\omega}|B}{2(v_{max} - v_{min})}, \quad (16)$$

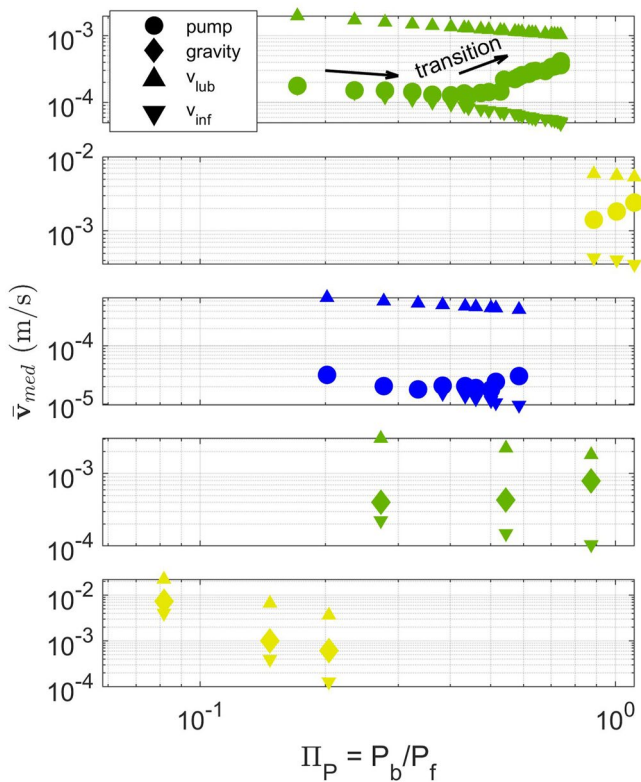


Figure 4. Velocity measurements (circles or diamonds) in comparison with the superficial influx velocity and lubrication velocity scales (triangles). Measurements approach one scale or the other depending on the ratio of buoyancy to fracture pressure. Plots from top to bottom are respectively for experiments C1 to C5. Colors indicate the relative flux, high (yellow), medium (green) or low (blue).

ily due to the velocity field. We can then define a flow pattern parameter, Π_Q , using the mean values of Q_a and Q_d , averaged over the vertical length of the dike:

$$\Pi_Q = \frac{|\overline{Q_d}|}{\overline{Q_a}}, \quad (19)$$

which approaches either a value of 1 or 0, respectively for a circulating or ascending flow pattern. We compare Π_Q with Π_p and identify a clear, negative correlation for C series experiments and no clear correlation for S series experiments, both in agreement with qualitative observations (Figure 7a). As Π_p increases in C series experiments and the dike becomes buoyant ($\Pi_p \rightarrow 1$), the flow pattern becomes dominantly ascending ($\Pi_Q \rightarrow 0$).

We also compare Π_Q with Re , as it can characterize the dimensionless influx, but find no conclusive relationship between the two (Figure 7b). As previously stated in Section 3.1, experiments C1 through C3 (solid circles) all transitioned from a circulating to ascending flow pattern as their lengths approached L_b , even though their influxes (and thus Re) differed by orders of magnitude. There appears to be a positive correlation on an experiment-by-experiment basis (e.g., C1, solid green circles, is positively correlated), but this is likely due to dike growth, in that $Re \propto L^{-1}$.

As previously discussed, the S series data do not follow the same relationship as the C series, which is apparent in Figure 7a. As shown in Figure 2xi through xv, the liquid in the S series maintained a circulating flow pattern throughout propagation. This was especially evident in the dike's upper head, which was absent in isothermal dikes longer than the buoyancy length. We also observe the development of a high-velocity supply conduit in the tail, which connects the source to the dike head, presumably bypassing the otherwise-solidified (or possi-

and compare it to Π_p , we can see that there is no relationship between the two (Figure 6c).

We therefore conclude that vorticity is not the cause of the observed flow patterns. Dikes maintain a velocity gradient $\partial v/\partial x$ that generates vorticity, regardless of buoyancy. When the average ascent velocity is less than the vorticity, a circulating flow pattern is observed (e.g., Figure 2vi), but when it is greater, an ascending flow pattern is observed (e.g., Figure 2iii).

3.4. Ascending and Descending Flux

As we see in Figure 2, a circulating flow pattern occurs when there is upward and downward liquid movement. In order to quantify the flow pattern, we use the ascending and descending flux, respectively Q_a and Q_d . These are vary with vertical position in the dike and are defined as,

$$Q_a(z) = \sum [v(x, z) > 0] H(x, z) \Delta x, \quad (17)$$

and

$$Q_d(z) = \sum [v(x, z) < 0] H(x, z) \Delta x, \quad (18)$$

where Δx is the size of a pixel. Note that the PIV technique inhibits measuring the thickness distribution, which can otherwise be obtained using the amount of light transmitted through a pigmented dike (e.g., Taisne et al., 2011). We therefore need to make an assumption on how the thickness varies as a function of position within the dike. We could model the thickness distribution as an inverted tear drop, which is valid for buoyant dikes, or as a penny-shaped crack, which is valid for non-buoyant dikes (Menand & Tait, 2002; Rivalta & Dahm, 2006; Rivalta et al., 2005), but would need to make additional assumptions on how the dike transitions from one shape to the other. As such, we simplify the geometry to a uniform thickness of $H \sim 4 V/\pi LB$ and assume variations in vertical flux are primarily

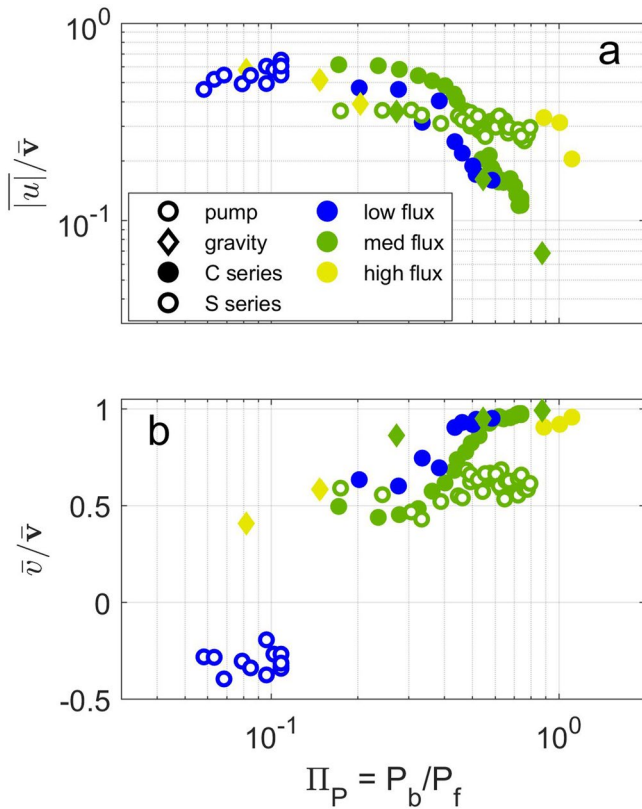


Figure 5. (a) The mean of the absolute value of horizontal velocity, scaled to the mean velocity vector, shown against Π_P . C series data shows a strong negative correlation with Π_P , whereas the S series varies less with Π_P . (b) A similar plot for the vertical component. We use a linear vertical axis as some S series data has a negative value, as the return flow covers a much larger area of the dike than the upward flow.

bly high-viscosity) tail. We interpret that the high liquid velocity exiting the conduit stirs up the liquid in the larger head region, prolonging circulation. However, we cannot rule out the possibility that the circulation is primarily due to viscosity variations between the hottest and coolest liquid gelatin, in that a large viscosity ratio between the two can lead to a heterogeneous flow field.

4. PTV Analysis

These experiments provide the capability to track individual tracer particles and visualize their flow paths, via particle tracking velocimetry (PTV). We processed our video recordings in a Matlab-based (The Mathworks Inc., 2019) PTV toolbox, developed by Hedrick (2008). We tracked several particles for a buoyantly propagating dike (experiment C1) and for a non-buoyant dike (experiment S3), for both the propagation phase of liquid flow and for the post-eruptive phase of flow. We chose C1 (out of C1 through C4, which had similar ascending flow patterns) and S3 (out of C5 and S3, which had similar circulating flow patterns) due to their relatively low particle seeding concentrations, which facilitates particle tracking. High concentrations can cause particles to overlap one another, which interferes with automated detection of particle locations.

In the case of a non-buoyant dike (Figures 8a and 8b), the particles exhibited circulation and oscillated between shallow and deep several times, though they did not necessarily descend to the bottom of the dike. Particles ascended along the dike's central upward flow path, then traveled in an arc along the upper tip and finally migrated downward, before being entrained into the ascending flow again. Particles display variable velocity, evident in the slope of the curves in Figure 8b, which are steep when ascending and more gradual when descending. We also observe that the particles took longer to complete a revolution as the dike grew, which in Figure 8b appears as the oscillation wavelength becoming longer toward the right side of the graph. Particles injected toward the beginning of propagation oscillated a greater number of times than those injected later. Note that some particles became stuck in the gelatin due to solidification (marked with an \times in Figures 8a and 8b), while others were able to erupt. After the eruption began, particles then took on a simple, ascending path.

In the case of a buoyant dike (Figures 8c and 8d), the particle tracking shows little circulation and instead indicates vertical movement toward the upper tip, followed by lateral movement toward the sides of the dike. We

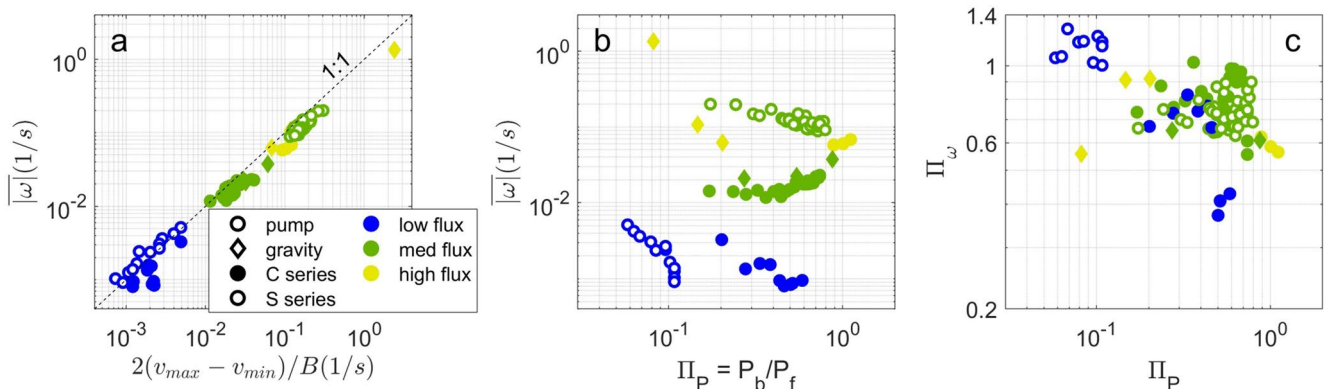


Figure 6. (a) The median of the absolute value of vorticity measurements, against the difference between maximum and minimum velocity, scaled to dike size. There is a clear relationship between the parameters. (b) The same against Π_P , shows no consistent relationship between vorticity and buoyancy for C series experiments, but does show negative correlations with the S series. (c) The dimensionless parameter Π_ω shows no obvious relationship with Π_P .

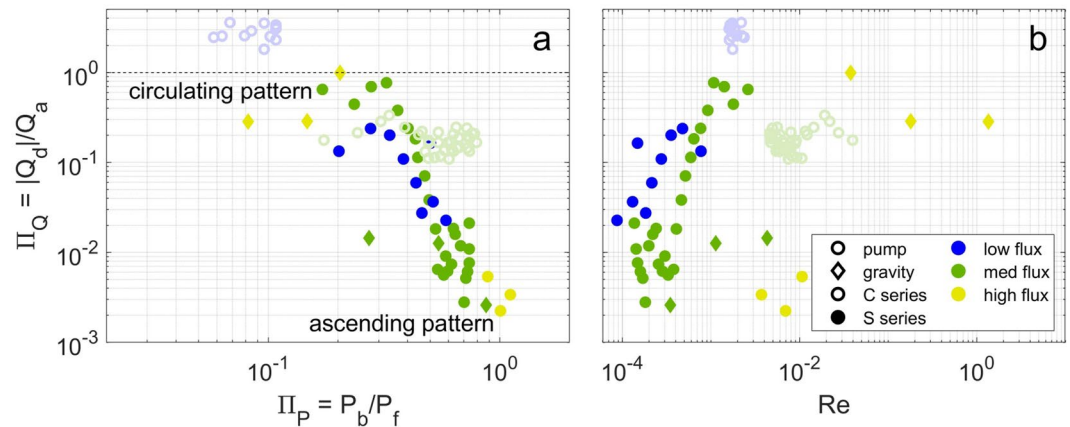


Figure 7. The flow pattern parameter, Π_Q , against (a) the dimensionless buoyancy, Π_P , and (b) the Reynolds number. The S series data have been faded to highlight the isothermal C series. The horizontal dashed line in (a) is a hypothetical maximum value, in which ascending and descending flux are the same magnitude. There is a negative correlation for C series experiments in (a), but no consistent relationship in (b).

suspect that once particles reach the top, continuous influx from below pushed them toward the sides, where they could occupy newly fractured space. Once at the side, they temporarily decelerated, then accelerated upwards as the dike's buoyancy increased. After the onset of eruption, particles simply ascended toward the vent. Some particles show a marked change in direction at the onset of eruption (e.g., Figure 8c, particle "1").

We want to know if there is any relationship between the complexity of a particle's path and when it is ejected from the dike. The path complexity can be quantified by the total path length, L_p , which we estimate by summing the change of position over the entire sequence. This is normalized to the depth of the source reservoir (thus final dike length), L , and compared with the time it is ejected, t_{eject} , normalized to the time of eruption onset, t_{erupt}

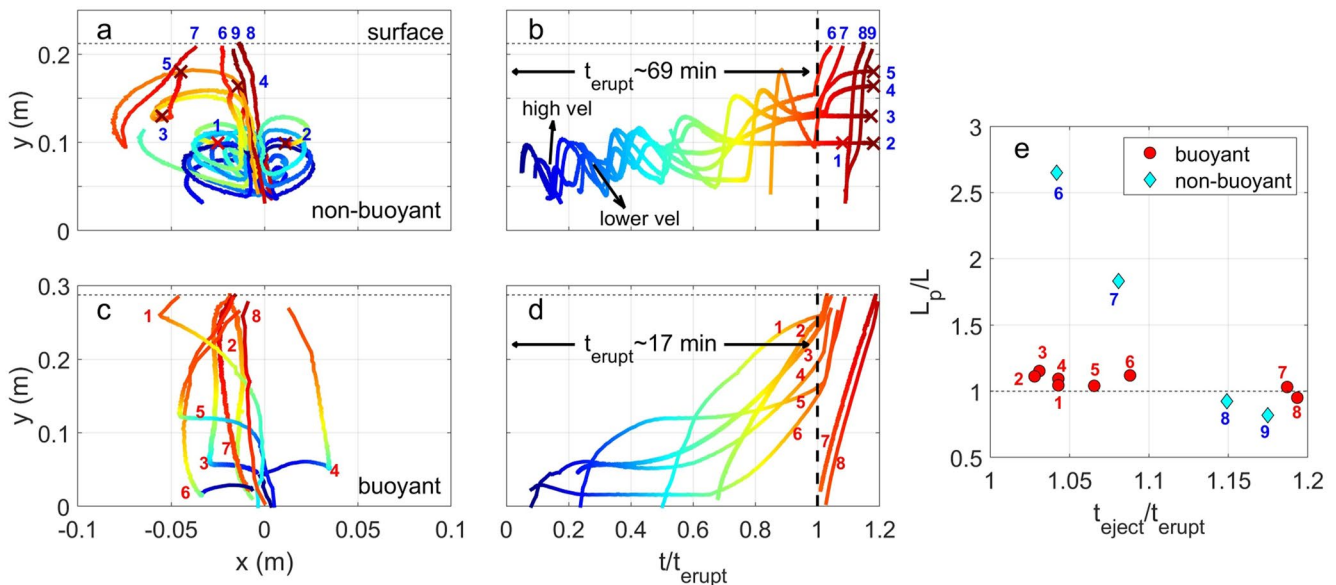


Figure 8. (a, b) Particle tracking results for a non-buoyant dike (experiment S3) and (c, d) buoyant dike (experiment C1). The left panels show particle movement in 2D space, in which the color represents time. The center panels show the vertical position against time, normalized by the time of eruption, which is marked by a vertical dashed line. Note, the eruption time is strongly dependent on the influx (69 min for S3, $Q = 3$ mL/min; 17 min for C1, $Q = 11$ mL/min). Some particles did not erupt and instead were trapped during solidification (indicated by an \times marking). (e) Particle path lengths, L_p , normalized to dike length, L , are shown against the time they are ejected, t_{eject} , normalized to the eruption time. Particles that did not erupt are not shown. Particles that circulated more have a high L_p/L and were the first to erupt. Note that some points with $L_p/L < 1$ occur, since particle tracking does not always begin precisely at the bottom of the dike (so the particle path appears shorter than the dike length).

(Figure 8e). For the non-buoyant S3, the first particles to exit (smallest $t_{\text{eject}}/t_{\text{erupt}}$) were inside the dike during propagation and therefore circulated more (largest L_p/L). The last particles to exit tended to enter the dike after eruption began. These flowed directly to the surface and had L_p/L approaching 1. Note some values are less than 1, as tracking was not necessarily started precisely at the dike bottom. For the buoyant dike, most particles had L_p/L approaching 1, regardless of ejection time.

5. Discussion

5.1. Linking PTV Results to Crystal Growth Patterns

We first discuss our PTV findings in the context of crystal growth. While the particles are too large to be geometrically scaled to a crystal, both particles and crystals are coupled to the liquid flow, and thus passively follow the fluid dynamics.

The flow dynamics during propagation can potentially be recorded in crystal textures, in which layers indicate the physical and chemical conditions in which they grow, while diffusion profiles indicate the associated time scales (Gordeychik et al., 2018). For a crystal to record changes in environment, it needs sufficient time to grow a layer. It is possible that magma dynamics like circulation promote homogenization of the magma, so the resulting crystals would be homogeneous. However, we argue that a crystal entrained in a propagating dike would be subjected to rapidly changing pressure conditions, especially if it ascends and descends multiple times. Similarly, it would be subjected to variable temperature conditions as it moves between hotter, central regions where magma first enters the dike and the cooler outer peripheries. For a dike to be thermally homogeneous, we expect the circulation would have to be extremely high to supersede the efficient cooling from a dike, which is, by definition, thin with a large surface area. Indeed, recent studies have shown that olivine crystals can record information of a variable environment, on the time scale of a propagating dike (Albert et al., 2020; Cheng et al., 2020; Gordeychik et al., 2018).

If a crystal were entrained in analogous magmatic dike to experiment S3 (Figures 8a and 8b), we would expect to see oscillatory growth patterns associated with the cyclic changes in pressure and temperature. The number of layers could indicate if the crystal was injected earlier or later in the propagation, and we would expect the thickness of layers to increase as the dike grew, as particles took longer to complete a revolution as the dike grew. Crystals injected after the onset of eruption would likely show a simpler growth pattern, which reflects the rapid change of conditions between the source and the surface.

For a crystal in an analogous magmatic dike to experiment C1 (Figures 8c and 8d), the pattern would likely be simpler than in the previous example. The temporary drop in velocity as the magma is pushed toward the side of the dike favors the growth of a distinct layer, associated with the pressure and temperature conditions at that location. As such a dike continues to grow, crystals would resume ascent and potentially record a gradual change of conditions, associated with the diminishing pressure.

We argue that the petrologic samples taken just after the onset of eruption can distinguish the flow pattern and potentially the dominant driving pressure during propagation. In the PTV measurements (Figure 8e, data with $t_{\text{eject}}/t_{\text{erupt}}$ approaching 1), particles in the non-buoyant dike circulated several times (largest L_p/L), whereas those in the buoyant dike ascended in a relatively direct manner (L_p/L approaching 1). After eruption, all particles assume a direct path from source to surface, so the flow dynamics would no longer be distinguishable.

It should be reiterated that experiments S1 and S2 maintained a circulating pattern, even after becoming buoyant. This indicates that other factors, like flow localization in the dike tail, can promote circulation. Therefore, crystals might provide insight into the flow dynamics inside a dike, but not decisively prove the cause of those dynamics. We suggest comparing petrologic data, in which oscillations may provide some information on the size of the dike head, with geophysical data (e.g., earthquake locations, ground deformation data), which can provide information on the total dike dimensions. If crystals suggest a smaller length scale of oscillation than the size of the dike, this could be evidence for a constrained circulating region like that shown in experiment S2 (Figure 2xiii).

5.2. A Model of Dike Growth and Circulation

Based in part on observations from our experiments, we develop a conceptual model of magma circulation coupled with dike propagation. Our experimental results indicate that: (a) buoyancy inhibits circulation and

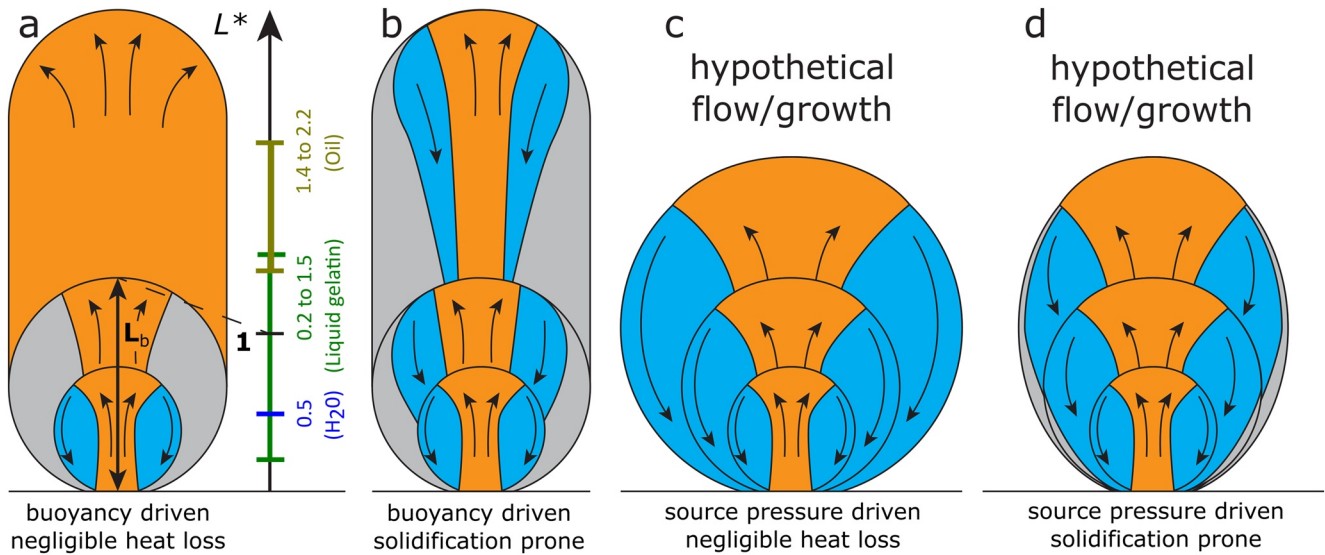


Figure 9. Conceptual illustrations of different propagation dynamics. Orange, blue and gray respectively represent upward, downward and negligible flow. (a) Dikes transition between flow patterns as buoyancy becomes dominant, as $L^* \rightarrow 1$. Also shown are estimates of L^* for our experiments ($L^* = L/L_b$). (b) A similar dike with significant heat loss and solidification. The tail partially solidifies, generating a conduit. Circulation is maintained in the head. (c, d) Similar illustrations for dikes driven by source pressure, in which circulation is maintained. Solidification constrains the horizontal growth to some degree.

drives ascending flow and vertical dike growth, which dominates as Π_p approaches a value of 1 (Figure 7a shows a negative trend between Π_p and Π_Q); (b) conversely, a dominant source pressure likely drives circulation and radial dike growth (c) the Re , which characterizes influx (not to be confused with source pressure), does not control the magma flow pattern (Figure 7b shows no overall trend between Re and Π_Q); and (d) solidification favors circulation in the head of the dike, due to flow localization in the tail.

The observed change in flow pattern occurred when $P_b \sim P_p$ but as stated in the scaling section, P_f is likely balanced with the total driving pressure, so that $P_f \sim \Delta P + P_b$; therefore, the change occurs when $P_b \gg \Delta P$. This is consistent with findings by Menand and Tait (2002), who argue radial propagation (maintaining a penny-shape) occurs when $\Delta P > P_b$ and vertical propagation when $P_b > \Delta P$, which changes when $P_b \sim \Delta P$. In our experiments, the peristaltic pump supplies whatever pressure is needed to maintain a constant flux, so the ΔP is large at the beginning of an experiment, but diminishes as buoyancy takes over. The gravity-driven experiment C5 (with water) never became buoyant, so $\Delta P \sim P_f > P_b$. For the gravity-driven experiment C4 (with oil), the pressure head balanced with viscous pressure drop in the supply tubing, effectively yielding a constant-flux, variable-pressure experiment, replicating the conditions of the pump.

Putting this information together, we expect that all dikes have an initial phase of internal circulation driven by source pressure. If buoyancy becomes dominant, they transition to an ascending flow pattern with vertical growth (Figure 9a). If cooling is non-negligible, solidification in the tail modifies the flow pattern, localizing flow within the tail and circulating in the head (Figure 9b). For dikes with a dominant source pressure (or negligible buoyancy), the dike maintains a circulating flow pattern throughout propagation, with radial growth (Figure 9c). When solidification is non-negligible, we expect solidification at the sides somewhat limits the horizontal growth (Figure 9d).

5.3. Horizontally Propagating Dikes

Our experiments were configured to analyze continuously injected, vertically propagating dikes in a homogeneous medium. However, many dikes in nature are observed to propagate sub-horizontally: intrusions at spreading centers (Fialko & Rubin, 1998); dikes in a volcano's associated rift zones (Michon et al., 2015; Wright & Marsh, 2016); dikes propagating from an edifice as a flank eruptions (Caudron et al., 2015; Gudmundsson et al., 2014; Lundgren et al., 2015), to name a few. Analogue and numerical models show that this can occur due to density, rheological or stress barriers, which inhibit vertical propagation (Lister & Kerr, 1991; Menand et al., 2010; Rivalta et al., 2005). An ascending dike may experience some or all of these factors as they approach

the surface and encounter rock layers of contrasting rheology to the basement rocks (Geishi et al., 2012; Taisne & Jaupart, 2009) and/or local stresses due to an edifice's load (Pinel & Jaupart, 2004). Our experiments were not designed to study lateral propagation, so future work is needed to explore the internal flow characteristics in such dikes.

5.4. Viscous Versus Fracture Dominated Dikes

Analogue experiments in gelatin tend to have dominant elastic and fracture pressures, and negligible viscous pressure drop (Menand & Tait, 2002; Pansino et al., 2022). In basaltic dikes, it is debatable whether the fracture pressure or viscous pressure drop limits propagation (Rivalta et al., 2015). Laboratory measurements of the fracture toughness of mafic rocks yield values of $1 < K_c < 3 \text{ MPa} \cdot \text{m}^{1/2}$ (Balme et al., 2004; Meredith & Atkinson, 1983, 1985), yet field measurements (presumably assuming $P_e \sim P_f$) indicate an effective value of $K_c \sim 100 \text{ MPa} \cdot \text{m}^{1/2}$ (Rivalta et al., 2015). If dikes in nature are dominated instead by viscous pressure drop and elastic pressure, then the fracture pressure would in fact be negligible, making it inappropriate for field analysis.

We can estimate a length scale, L_v , at which viscous pressure drop surpasses fracture pressure, which occurs when $P_e \sim P_f \sim P_v$. The thickness H at this moment can be estimated via $P_e \sim P_v$, so that

$$H \sim \left[\frac{12\mu QL(1-\nu)}{G} \right]^{1/4}. \quad (20)$$

Substituting this into the equation for P_e (Equation 3), and setting $P_e \sim P_f$, then

$$B \sim \left[\frac{12\mu QLG^3}{K_c^4(1-\nu)^3} \right]^{1/2}. \quad (21)$$

The breadth can be approximated to the buoyancy length (Equation 5), so that $B \sim L_b$, and therefore,

$$L_v \sim \frac{1}{12\mu Q} \left[\frac{1-\nu}{G} \right]^3 \left[\frac{K_c^{16}}{(\Delta\rho g)^4} \right]^{1/3}. \quad (22)$$

For the values for basaltic dikes listed in Table 2 (assuming laboratory measurements of K_c are correct), $L_v \ll 1 \text{ m}$, indicating dikes are effectively dominated by P_v and P_e from the moment they begin propagating. In experiments, using values from Table 1, $40 < L_v < 5 \times 10^5 \text{ m}$, verifying that they are never viscously dominated in our relatively small, $0.5 \times 0.5 \times 0.5 \text{ m}^3$ tank, and are instead influenced by P_f and P_e .

This suggests the need for experiments that achieve a dominant viscous pressure drop, which presumably can be accomplished with higher viscosity liquids and high-pressure pumps. We can restructure Equation 22 to solve for a combined μQ parameter to help select a liquid viscosity and pump speed. The G should be relatively high (here we will assume $G \sim 10^4 \text{ Pa}$) and L_v should be smaller than the size of a tank (we will assume $L_v = 15 \text{ cm}$) in order to observe the transition from fracture to viscous dominated propagation. Silicone oils have a density similar to water, so that $\Delta\rho \sim 10 \text{ kg/m}^3$, but have a wide range of viscosities that offer flexibility for experiments. Taking these parameters, and $K_c \propto G^{1/2}$, then the combined μQ is $8 \times 10^{-4} \text{ Pa} \cdot \text{m}^3$, which could be achieved using a silicone oil with $\mu = 100 \text{ Pa} \cdot \text{s}$ and influx $Q = 8 \text{ mL/s}$. It is also possible to mix additives like salt into the gelatin to increase its density, potentially favoring a smaller L_v , however these can also affect the shear modulus and fracture toughness, potentially undoing any gains due to buoyancy; for example, salt increases the K_c and decreases G (Brizzi et al., 2016; Smittarello et al., 2021), both of which increase L_v .

6. Conclusion

We performed a series of analogue experiments to determine the driving forces that control the internal flow in a propagating dike. By injecting liquids of various rheologies (water, oil and liquid gelatin) at varying flux rates, we determined that the internal flow dynamics change depending on the driving forces. Non-buoyant, isothermal dikes take on a circulating pattern, while buoyant, isothermal dikes take on an ascending one. As dikes erupt, they deflate and expel much of their volumes onto the surface, after which internal flow rapidly transitions to a steady flow from source to surface. This change occurs as the dimensionless parameters Π_p approaches a value

of 1. The Reynolds number does not appear to play a role, in that high fluxes drive faster flow, but the overall pattern remains unaffected.

Solidification affects the flow field, prolonging circulation in the dike head, even as the dike becomes buoyant. We suspect this is due to solidification of the dike tail, which contains a liquid supply conduit that connects the source to the dike head. The conduit sustains a high flow velocity, which we argue stirs up circulation.

In the context of natural systems, we posit that crystals in erupted lavas may provide some insight on whether a dike is driven by buoyancy or source pressure. For example, oscillatory zoned crystals have been shown to record fluctuating conditions that could be associated with a circulating pattern, which in turn provides evidence of a source-pressure controlled dike. Crystals with normal zoning could be associated with either buoyant propagation or erupting magma. By comparing petrologic evidence with dike dimensions, obtained through geophysical data, the driving forces acting on a dike can be determined with a good degree of confidence.

Data Availability Statement

Our data is available at <https://doi.org/10.7910/DVN/QISP4Y>, under Harvard Dataverse.

Acknowledgments

This work comprises Earth Observatory of Singapore contribution no. 313. This research is supported by the National Research Foundation Singapore (award NRF2015-NRF-ISF001-2437) and the Singapore Ministry of Education under the Research Centres of Excellence initiative. S. Pansino was funded by a Newton International Fellowship (award NIFAR1/202137), supported by the Royal Society.

References

- Adrian, R. J. (1991). Particle-imaging techniques for experimental fluid mechanics. *Annual Review of Fluid Mechanics*, 23(1), 261–304. <https://doi.org/10.1146/annurev.fl.23.010191.001401>
- Albert, H., Larrea, P., Costa, F., Widom, E., & Siebe, C. (2020). Crystals reveal magma convection and melt transport in dyke-fed eruptions. *Nature Scientific Reports*, 10(1), 11632. <https://doi.org/10.1038/s41598-020-68421-4>
- Balme, M. R., Rocchi, V., Jones, C., Sammonds, P. R., Meredith, P. G., & Boon, S. (2004). Fracture toughness measurements on igneous rocks using a high-pressure, high-temperature rock fracture mechanics cell. *Journal of Volcanology and Geothermal Research*, 132(2–3), 159–172. [https://doi.org/10.1016/S0377-0273\(03\)00343-3](https://doi.org/10.1016/S0377-0273(03)00343-3)
- Brizzi, S., Funicello, F., Corbi, F., Di Giuseppe, E., & Mojoli, G. (2016). Salt matters: How salt affects the rheological and physical properties of gelatine for analogue modelling. *Tectonophysics*, 679, 88–101. <https://doi.org/10.1016/j.tecto.2016.04.021>
- Caudron, C., Tainse, B., Kugaenko, Y., & Saltykov, V. (2015). Magma migration at the onset of the 2012–2013 Tolbachik eruption revealed by Seismic Amplitude Ratio Analysis. *Journal of Volcanology and Geothermal Research*, 307, 60–67. <https://doi.org/10.1016/j.jvolgeores.2015.09.010>
- Cheng, L., Costa, F., & Bergantz, G. (2020). Linking fluid dynamics and olivine crystal scale zoning during simulated magma intrusion. *Contributions to Mineralogy and Petrology*, 175(6), 53. <https://doi.org/10.1007/s00410-020-01691-3>
- Choi, Y. H., Lim, S. T., & Yoo, B. (2004). Measurement of dynamic rheology during ageing of gelatine–sugar composites. *International Journal of Food Science and Technology*, 39(9), 935–945. <https://doi.org/10.1111/j.1365-621.2004.00871.x>
- Coote, A., Shane, P., Stirling, C., & Reid, M. (2018). The origin of plagioclase phenocrysts in basalts from continental monogenetic volcanoes of the Kaikohe-Bay of Islands field, New Zealand: Implications for magmatic assembly and ascent. *Contributions to Mineralogy and Petrology*, 173(2), 14. <https://doi.org/10.1007/s00410-018-1440-y>
- Crabtree, S. M., & Waters, L. E. (2017). The petrologic history of the Sanganguey volcanic field, Nayarit, Mexico: Comparisons in a suite of crystal-rich and crystal-poor lavas. *Journal of Volcanology and Geothermal Research*, 336, 51–67. <https://doi.org/10.1016/j.jvolgeores.2017.02.005>
- Delaney, P. T., & Pollard, D. D. (1982). Solidification of basaltic magma during flow in a dike. *American Journal of Science*, 282(6), 856–885. <https://doi.org/10.2475/ajs.282.6.856>
- Douglas, M. M., Geyer, A., Álvarez-Valero, A. M., & Martí, J. (2016). Modeling magmatic accumulations in the upper crust: Metamorphic implications for the country rock. *Journal of Volcanology and Geothermal Research*, 319, 78–92. <https://doi.org/10.1016/j.jvolgeores.2016.03.008>
- Fialko, Y. A., & Rubin, A. M. (1998). Thermodynamics of lateral dike propagation: Implications for crustal accretion at slow spreading mid-ocean ridges. *Journal of Geophysical Research*, 103(B2), 2501–2514. <https://doi.org/10.1029/97JB03105>
- Geishi, N., Kusumoto, S., & Gudmundsson, A. (2012). Effects of mechanical layering of host rocks on dike growth and arrest. *Journal of Volcanology and Geothermal Research*, 223–224, 74–82. <https://doi.org/10.1016/j.jvolgeores.2012.02.004>
- Gordeychik, B., Churikova, T., Kronz, A., Sundermeyer, C., Simakin, A., & Wörner, G. (2018). Growth of, and diffusion in, olivine in ultra-fast ascending basalt magmas from Shiveluch volcano. *Scientific Reports*, 8(1), 11775. <https://doi.org/10.1038/s41598-018-30133-1>
- Gudmundsson, A., Lecœur, N., Mohajeri, N., & Thordarson, T. (2014). Dike emplacement at Bardarbunga, Iceland, induces unusual stress changes, caldera deformation, and earthquakes. *Bulletin of Volcanology*, 76(10), 869. <https://doi.org/10.1007/s00445-014-0869-8>
- Hedrick, T. L. (2008). Software techniques for two- and three-dimensional kinematic measurements of biological and biomimetic systems. *Bioinspiration & Biomimetics*, 3, 034001. <https://doi.org/10.1088/1748-3182/3/3/034001>
- Jones, T. J., & Llewellyn, E. W. (2021). Convective tipping point initiates localization of basaltic fissure eruptions. *Earth and Planetary Science Letters*, 553, 116637. <https://doi.org/10.1016/j.epsl.2020.116637>
- Kavanagh, J. L., Burns, A. J., Hazim, S. H., Wood, E. P., Martin, S. A., Hignett, S., & Dennis, D. (2018). Challenging dyke ascent models using novel laboratory experiments: Implications for reinterpreting evidence of magma ascent and volcanism. *Journal of Volcanology and Geothermal Research*, 354, 87–101. <https://doi.org/10.1016/j.jvolgeores.2018.01.002>
- Kavanagh, J. L., Menand, T., & Daniels, K. A. (2013). Gelatine as a crustal analogue: Determining elastic properties for modelling magmatic intrusions. *Tectonophysics*, 582, 101–111. <https://doi.org/10.1016/j.tecto.2012.09.032>
- Keating, G. N., Valentine, G. A., Krier, D. J., & Perry, F. V. (2008). Shallow plumbing systems for small-volume basaltic volcanoes. *Bulletin of Volcanology*, 70(5), 563–582. <https://doi.org/10.1007/s00445-007-0154-1>

- Lee, B. J., Kee, S.-H., Oh, T., & Kim, Y.-Y. (2017). Evaluating the dynamic elastic modulus of concrete using shear-wave velocity measurements. *Advances in Materials Science and Engineering*, 2017, 1651753. <https://doi.org/10.1155/2017/1651753>
- Lister, J. R. (1990). Buoyancy-driven fluid fracture: Similarity solutions for the horizontal and vertical propagation of fluid-filled cracks. *Journal of Fluid Mechanics*, 217, 213–239. <https://doi.org/10.1017/S0022112090000696>
- Lister, J. R., & Kerr, R. C. (1991). Fluid-mechanical models of crack propagation and their application to magma transport in dykes. *Journal of Geophysical Research*, 96(B6), 10049–10077. <https://doi.org/10.1029/91jb00600>
- Lundgren, P., Kiryukhin, A., Milillo, P., & Samsonov, S. (2015). Dike model for the 2012–2013 Tolbachik eruption constrained by satellite radar interferometry observations. *Journal of Volcanology and Geothermal Research*, 307, 79–88. <https://doi.org/10.1016/j.jvolgeores.2015.05.011>
- Menand, T., Daniels, K. A., & Benghiat, P. (2010). Dyke propagation and sill formation in a compressive tectonic environment. *Journal of Geophysical Research*, 115(B8), B08201. <https://doi.org/10.1029/2009JB006791>
- Menand, T., & Tait, S. (2002). The propagation of a buoyant liquid-filled fissure from a source under constant pressure: An experimental approach. *Journal of Geophysical Research*, 107(B11), 2306. <https://doi.org/10.1029/2001JB000589>
- Meredith, P. G., & Atkinson, B. K. (1983). Stress corrosion and acoustic emission during tensile crack propagation in Whin Sill dolerite and other basic rocks. *Geophysical Journal of the Royal Astronomical Society*, 75, 1–21. <https://doi.org/10.1111/j.1365-246X.1983.tb01911.x>
- Meredith, P. G., & Atkinson, B. K. (1985). Fracture toughness and subcritical crack growth during high-temperature tensile deformation of West-erly granite and Black gabbro. *Physics of the Earth and Planetary Interiors*, 39(1), 33–51. [https://doi.org/10.1016/0031-9201\(85\)90113-X](https://doi.org/10.1016/0031-9201(85)90113-X)
- Michon, L., Ferrazzini, V., Di Muro, A., Villeneuve, N., & Famin, V. (2015). Rift zones and magma plumbing system of Piton de la Four-naise volcano: How do they differ from Hawaii and Etna? *Journal of Volcanology and Geothermal Research*, 303, 112–129. <https://doi.org/10.1016/j.jvolgeores.2015.07.031>
- Pansino, S., Emadzadeh, A., & Taisne, B. (2022). Modeling dike propagation in both vertical length and horizontal breadth. *Journal of Geophys-ical Research*, 127(10), e2022JB024593. <https://doi.org/10.1029/2022JB024593>
- Pansino, S., Emadzadeh, E., & Taisne, B. (2019). Dike channelization and solidification: Time scale controls on the geometry and placement of magma migration pathways. *Journal of Geophysical Research*, 124(9), 9580–9599. <https://doi.org/10.1029/2019JB018191>
- Pansino, S., & Taisne, B. (2019). How magmatic storage regions attract and repel propagating dikes. *Journal of Geophysical Research*, 124(1), 274–290. <https://doi.org/10.1029/2018JB016311>
- Pansino, S., & Taisne, B. (2020). Shear wave measurements of a Gelatin's Young's modulus. *Frontiers of Earth Science*, 8, 171. <https://doi.org/10.3389/feart.2020.00171>
- Pinel, V., & Jaupart, C. (2004). Magma storage and horizontal dyke injection beneath a volcanic edifice. *Earth and Planetary Science Letters*, 221(1–4), 245–262. [https://doi.org/10.1016/S0012-821X\(04\)00076-7](https://doi.org/10.1016/S0012-821X(04)00076-7)
- Raffel, M., Willert, C. E., & Kompenhans, J. (2013). *Particle image velocimetry: A practical guide*. Springer.
- Rivalta, E., Bottinger, M., & Dahm, T. (2005). Buoyancy-driven fracture ascent: Experiments in layered gelatin. *Journal of Volcanology and Geothermal Research*, 144(1–4), 273–285. <https://doi.org/10.1016/j.jvolgeores.2004.11.030>
- Rivalta, E., & Dahm, T. (2006). Acceleration of buoyancy-driven fractures and magmatic dikes beneath the free surface. *Geophysical Journal International*, 166(3), 1424–1439. <https://doi.org/10.1111/j.1365-246X.2006.02962.x>
- Rivalta, E., Taisne, B., Bungler, A., & Katz, R. (2015). A review of the mechanical models of dike propagation: Schools of thought, results and future directions. *Tectonophysics*, 638, 1–42. <https://doi.org/10.1016/j.tecto.2014.10.003>
- Roper, S., & Lister, J. R. (2007). Buoyancy-driven crack propagation: The limit of large fracture toughness. *Journal of Fluid Mechanics*, 580, 359–380. <https://doi.org/10.1017/S0022112007005472>
- Schlichting, H., & Gersten, K. (2017). *Boundary-layer theory* (9th ed.). Springer Berlin. <https://doi.org/10.1007/978-3-662-52919-5>
- Schonwalder-Angel, D., Cortés, J. A., & Calder, E. S. (2018). The interplay of magmatism and tectonics: An example based on the satellite scoria cones at Llaïma volcano, Chile. *Journal of Volcanology and Geothermal Research*, 367, 31–45. <https://doi.org/10.1016/j.jvolgeores.2018.10.020>
- Schroeder, A., & Willert, C. E. (2008). *Particle image velocimetry: New developments and recent applications*. Springer.
- Smittarello, D., Pinel, V., Maccaferri, F., Furst, S., Rivalta, E., & Cayol, V. (2021). Characterizing the physical properties of gelatin, a classic analog for the brittle elastic crust, insight from numerical modeling. *Tectonophysics*, 812, 228901. <https://doi.org/10.1016/j.tecto.2021.228901>
- Taisne, B., & Jaupart, C. (2009). Dike propagation through layered rocks. *Journal of Geophysical Research*, 114(B9), B09203. <https://doi.org/10.1029/2008JB06228>
- Taisne, B., & Tait, S. (2011). Effect of solidification on a propagating dike. *Journal of Geophysical Research*, 116(B1), B01206. <https://doi.org/10.1029/2009JB007058>
- Taisne, B., Tait, S., & Jaupart, C. (2011). Conditions for the arrest of a vertical propagating dyke. *Bulletin of Volcanology*, 73(2), 191–204. <https://doi.org/10.1007/s00445-010-0440-1>
- The MathWorks Inc. (2019). MATLAB version: 9.7.0.1190202 (R2019b). The MathWorks Inc. Retrieved from <https://www.mathworks.com>
- Traversa, P., Pinel, V., & Grasso, J. R. (2010). A constant influx model for dike propagation: Implications for magma reservoir dynamics. *Journal of Geophysical Research*, 115(B1), B01201. <https://doi.org/10.1029/2009JB006559>
- Wada, Y. (1994). On the relationship between dike width and magma viscosity. *Journal of Geophysical Research*, 99(B9), 17743–17755. <https://doi.org/10.1029/94JB00929>
- Watanabe, T., Masuyama, T., Nagaoka, K., & Tahara, T. (2002). Analog experiments on magma-filled cracks: Competition between external stresses and internal pressure. *Earth Planets and Space*, 54(12), 1247–1261. <https://doi.org/10.1186/BF03352453>
- Whitehead, J. A., & Helfrich, K. R. (1991). Instability of flow with temperature-dependent viscosity: A model of magma dynamics. *Journal of Geophysical Research*, 96(B3), 4145–4155. <https://doi.org/10.1029/90JB02342>
- Wright, T. L., & Marsh, B. (2016). Quantification of the intrusion process at Kīlauea volcano, Hawai'i. *Journal of Volcanology and Geothermal Research*, 328, 34–44. <https://doi.org/10.1016/j.jvolgeores.2016.09.019>
- Zhang, P., & Porfiri, M. (2019). A combined digital image correlation/particle image velocimetry study of water-backed impact. *Composite Structures*, 224, 111010. <https://doi.org/10.1016/j.compstruct.2019.111010>

References From the Supporting Information

- Di Giuseppe, E., Funicello, F., Corbi, F., Ranalli, G., & Mojoli, G. (2009). Gelatins as rock analogs: A systematic study of their rheological and physical properties. *Tectonophysics*, 473(3–4), 391–403. <https://doi.org/10.1016/j.tecto.2009.03.012>
- Pang, Z., Deeth, H., Sopade, P., Sharma, R., & Bansal, N. (2014). Rheology, texture and microstructure of gelatin gels with and without milk proteins. *Food Hydrocolloids*, 35, 484–493. <https://doi.org/10.1016/j.foodhyd.2013.07.007>